

Mission Support for the Communication/Navigation Outage Forecast System (C/NOFS) Satellite

David L. Hysell

**Department of Earth and Atmospheric Sciences
Cornell University
2108 Snee Hall
Ithaca, NY 14853**

Final Report

21 November 2007

APPROVED FOR PUBLIC RELEASE; DISTRIBUTION UNLIMITED.



**AIR FORCE RESEARCH LABORATORY
Space Vehicles Directorate
29 Randolph Road
AIR FORCE MATERIEL COMMAND
Hanscom AFB, MA 01731-3010**

DTIC COPY

20080721 201

NOTICE AND SIGNATURE PAGE

Using Government drawings, specifications, or other data included in this document for any purpose other than Government procurement does not in any way obligate the U.S. Government. The fact that the Government formulated or supplied the drawings, specifications, or other data does not license the holder or any other person or corporation; or convey any rights or permission to manufacture, use, or sell any patented invention that may relate to them.

This report was cleared for public release and is available to the general public, including foreign nationals. Qualified requestors may obtain additional copies from the Defense Technical Information Center (DTIC) (<http://www.dtic.mil>). All others should apply to the National Technical Information Service.

AFRL-RV-HA-TR-2007-1189 HAS BEEN REVIEWED AND IS APPROVED FOR
PUBLICATION IN ACCORDANCE WITH ASSIGNED DISTRIBUTION STATEMENT.

//Signature//

JUDITH WELSH
Contract Manager

//Signature//

JOEL MOZER, Chief
Space Weather Center of Excellence

This report is published in the interest of scientific and technical information exchange, and its publication does not constitute the Government's approval or disapproval of its ideas or findings.

REPORT DOCUMENTATION PAGE

Form Approved
OMB No. 0704-0188

Public reporting burden for this collection of information is estimated to average 1 hour per response, including the time for reviewing instructions, searching existing data sources, gathering and maintaining the data needed, and completing and reviewing this collection of information. Send comments regarding this burden estimate or any other aspect of this collection of information, including suggestions for reducing this burden to Department of Defense, Washington Headquarters Services, Directorate for Information Operations and Reports (0704-0188), 1215 Jefferson Davis Highway, Suite 1204, Arlington, VA 22202-4302. Respondents should be aware that notwithstanding any other provision of law, no person shall be subject to any penalty for failing to comply with a collection of information if it does not display a currently valid OMB control number. PLEASE DO NOT RETURN YOUR FORM TO THE ABOVE ADDRESS.

1. REPORT DATE (DD-MM-YYYY)

21-11-2007

2. REPORT TYPE

Final Report

3. DATES COVERED (From - To)

Sept 2006 - Sept 2007

4. TITLE AND SUBTITLE

Mission Support for the Communication/Navigation Outage
Forecast System (C/NOFS) Satellite

5a. CONTRACT NUMBER

F19628-03-C-0067

5b. GRANT NUMBER**5c. PROGRAM ELEMENT NUMBER**

69120C

6. AUTHOR(S)

David L Hysell

5d. PROJECT NUMBER

1010

5e. TASK NUMBER

CN

5f. WORK UNIT NUMBER

A1

7. PERFORMING ORGANIZATION NAME(S) AND ADDRESS(ES)

Department of Earth and Atmospheric Sciences
Cornell University
2108 Snee Hall
Ithaca, NY 14853

8. PERFORMING ORGANIZATION REPORT NUMBER**9. SPONSORING / MONITORING AGENCY NAME(S) AND ADDRESS(ES)**

Air Force Research Laboratory
29 Randolph Road
Hanscom AFB, MA 01731-3010

10. SPONSOR/MONITOR'S ACRONYM(S)

AFRL/RVBXP

11. SPONSOR/MONITOR'S REPORT NUMBER(S)

AFRL-RV-HA-TR-2007-1189

12. DISTRIBUTION / AVAILABILITY STATEMENT

Approved for public release; distribution unlimited.

13. SUPPLEMENTARY NOTES**14. ABSTRACT**

Cornell University supported the Air Force Research Laboratory C/NOFS mission through a combination of experiment development, data acquisition and processing, simulation, and modeling of ionospheric processes pertinent to forecasting so-called equatorial spread F phenomena. A new radar mode capable of providing simultaneous plasma density and drift measurements in the equatorial ionosphere has been developed and implemented at the Jicamarca Radio Observatory. The new mode will be crucial for C/NOFS calibration/validation as well as for ongoing campaign support. Data acquired in this and other modes have been taken at Jicamarca in support of DMSP and COSMIC satellite overflights. Processed parameters have been posted and distributed to the C/NOFS science team through the Madrigal distributed data server. These data can also be used to test and initialize the AFRL forecast models. Additional experimental runs will be performed throughout the actual C/NOFS mission. Three specific investigations were carried out during the Cornell award period. An improved ionospheric irregularity forecast strategy based on an evolving understanding of a counterstreaming plasma instability process has been formulated. The new strategy should outperform traditional ones based solely on Rayleigh Taylor-type instability mechanisms. A new long-pulse incoherent scatter radar data processing scheme has been developed for improved measurement of plasma density, temperature, and composition profiles in the topside ionosphere. The new mode will be particularly useful right after C/NOFS launch, which will occur near solar minimum. A new means of inverting satellite radio occultation data has been developed and demonstrated. The method rejects artifacts that would otherwise obscure the E and valley regions and will increase the usefulness of beacon data from C/NOFS.

5. SUBJECT TERMS

CNOFS, ESF, Postsunset, Ionosphere, Irregularities, Radar

16. SECURITY CLASSIFICATION OF:**a. REPORT**

U

b. ABSTRACT

U

c. THIS PAGE

U

17. LIMITATION OF ABSTRACT

SAR

18. NUMBER OF PAGES

24

19a. NAME OF RESPONSIBLE PERSON

Judith A. Welsh

19b. TELEPHONE NUMBER (include area code)

Contents

1. INTRODUCTION	1
2. METHODS AND PROCEDURES	1
3. FINDINGS	2
4. BIBLIOGRAPHY	15

List of Figures

1. Six examples of ionospheric conditions around twilight. Each example shows the backscatter power (top panel), vertical plasma drift (middle panel), and zonal plasma drift (lower panel), plotted against the scales shown. Symbols plotted in the middle panel represent the vertical drift velocity at 450-km altitude for reference. The left and right columns portray events when topside spread F did not and did occur, respectively. Note that $UT = LT + 5h$ 3
2. Summary Jicamarca data for the full profile analysis. From top to bottom, the panels represent electron density, electron temperature, ion temperature, hydrogen ion fraction, and helium ion fraction (25% full scale). A data gap exists between 03-06 LT when the galaxy was directly over the radar. 7
3. Example occultation profile inversion comparing different methods. (a) Simulated "true" electron density profile $n_e(r)$. (b) Phase profile $\phi(s)$ calculated using (4). Simulated phase data with (solid) and without (dashed) noise are shown. (c) Direct linear inversion of the simulated data using (5). Models with (solid) and without (dashed) noise are shown. (d) Singular value analysis of the linear transformation (see text). (e) Linear inversion using Tikhonov regularization. The dashed line is the true model. (f) Results obtained using maximum entropy. The dashed line is the true model. 13

1. INTRODUCTION

This is a project to provide mission support for the Communication/Navigation Outage Forecast System (C/NOFS) under BAA VS-03-01 during its first four years of operation. The objective of the overall C/NOFS satellite mission is to develop and test methods for forecasting so-called equatorial spread F (ESF) events in the postsunset ionosphere associated with communications interruptions and to collect the data needed to do so on an operational basis. Cornell was to support the mission with ground-based radar observations of background ionospheric parameters and of ESF events from the Jicamarca Radio Observatory near Lima, Perú. Jicamarca is capable of measuring ionospheric electric field and conductivity profiles from the valley region well into the topside ionosphere. Jicamarca can also make very detailed observations of ionospheric irregularities associated with ESF. Three main tasks were to be supported under this project: (1) in-flight calibration of the electric field/drift meter sensors on board the spacecraft, (2) provision of Jicamarca radar support for experimental campaigns, both before the launch and during the satellite operations, and (3) analysis and interpretation of the data obtained during these campaigns in light of the C/NOFS mission goals.

2. METHODS AND PROCEDURES

The C/NOFS satellite is still on the ground awaiting launch. Consequently, the Cornell project underwent a series of redefinitions negotiated with our science counterparts at the Air Force Research Laboratory (AFRL). Some of our activities involved supporting other satellites, including DMSP and COSMIC. Many of the original objectives therefore carried over to these satellites. Data from Jicamarca were acquired, processed, and analyzed in conjunction with numerous DMSP and COSMIC passes during the project interval, and the results have been disseminated to the C/NOFS science team electronically and through meetings and workshops. In some instances, new techniques for satellite support were developed. Chief among these is a mode that measures calibrated plasma density and vector electric field profiles simultaneously. The various datasets are available for download now through the Madrigal UAF server. The C/NOFS satellite will receive comparable support for calibration, validation, and science operations upon launch.

Cornell was also charged with delivering ionospheric measurements to initialize and validate climatological, background, and forecast models under development at AFRL. These data were taken, processed, and made available. Finally, Cornell was to investigate ESF variability theoretically and to propose new forecast strategies based on our findings. This component of the project also proceeded as planned.

The results section of this report details outcomes from three specific investigations. These include 1) developing an improved forecast strategy for ESF based on our evolving understanding of a new class of dynamical plasma instabilities thought to initiate the phenomenon, 2) improving our analysis of Jicamarca long-pulse radar data to better support the radio occultation studies being performed with COSMIC as well as general-purpose DMSP, C/NOFS, and model calibration/validation (CalVal), and 3) investigating satellite radio occultation inversion strategies and proposing improvements rooted in contemporary practices. Each of these outcomes was already documented in separate publications.

3. FINDINGS

Findings pertaining to forecasting ESF based on a new instability model were presented in [31]. A new method of analyzing Jicamarca long-pulse radar data suitable for DMSP and C/NOFS CalVal and for validating COSMIC occultation measurements was described by [32]. Finally, an improved method for inverting satellite occultation data well suited for E and lower F region work was promoted by [28]. The most important findings are motivated and summarized below. Each of the following sections concludes with a recommendation for the ongoing C/NOFS mission.

3.1. Collisional Shear Instability and Equatorial Spread F

A striking characteristic of the bottomside F region ionosphere extending from late afternoon to a few hours before midnight is shear flow. Plasma drifts westward in the bottomside F region while drifting eastward near and above the F peak, with the shear being strongest just after sunset. That shear flow should exist in the bottomside equatorial F region was evident in the numerical modeling results of [22], argued on theoretical grounds by [10], and observed by [37] and [59]. This project focused attention on shear flow in the postsunset bottomside F region ionosphere and the possible role it plays in the variability of equatorial spread F .

While the existence of shear flow has been recognized for more than two decades, combined coherent and incoherent scatter observations at Jicamarca allowed us to locate the shear node and to assess the shear strength quantitatively for the first time (see Fig. 1). Shear flow exists for a period of several hours surrounding sunset and is most intense after sunset at low bottomside altitudes approaching the valley region. The scale length for the shear is measured in tens of kilometers there.

Shear flow arises mainly from the competition between the E and F region dynamos and from demands on the vertical boundary currents in the bottomside imposed from above by the imperfectly efficient F region dynamo and from below by interruptions in the equatorial electrojet around the evening terminator [20, 19]. Assessing the relative importance of these factors quantitatively is impeded by a lack of neutral wind profile measurements in the equatorial thermosphere as well as of off-equatorial E and valley region conductivities.

One consequence of vertical shear is the existence of regions where the zonal plasma flow is strongly retrograde, i.e., in the direction opposite the local neutral wind. When horizontal conductivity gradients are also present in such a region, wind-driven interchange instabilities and plasma irregularities result. This now appears to be the explanation for bottom-type scattering layers, which occupy retrograde strata and appear when the tilted postsunset F region supplies the necessary zonal conductivity gradient [35] (i.e. see the narrow layers in each panel of Fig. 1).

On occasions when topside spread F occurs, the bottom-type layers seem to be organized in clusters separated by tens or hundreds of km [31]. We know this from interferometric/imaging experiments at Jicamarca and also from coherent and incoherent scatter radar scans from the Altair radar on Kwajalein Atoll. We interpreted this modulation as evidence of intermediate and large-scale undulations or waves in the bottomside F region. The wind-driven instabilities would be stable and unstable in the different phases of such waves. In most instances, the topside irregularities that followed also exhibited structuring with the same characteristic scale size. The intermediate and large-scale waves therefore appear to serve as seed waves for full-blown spread F .

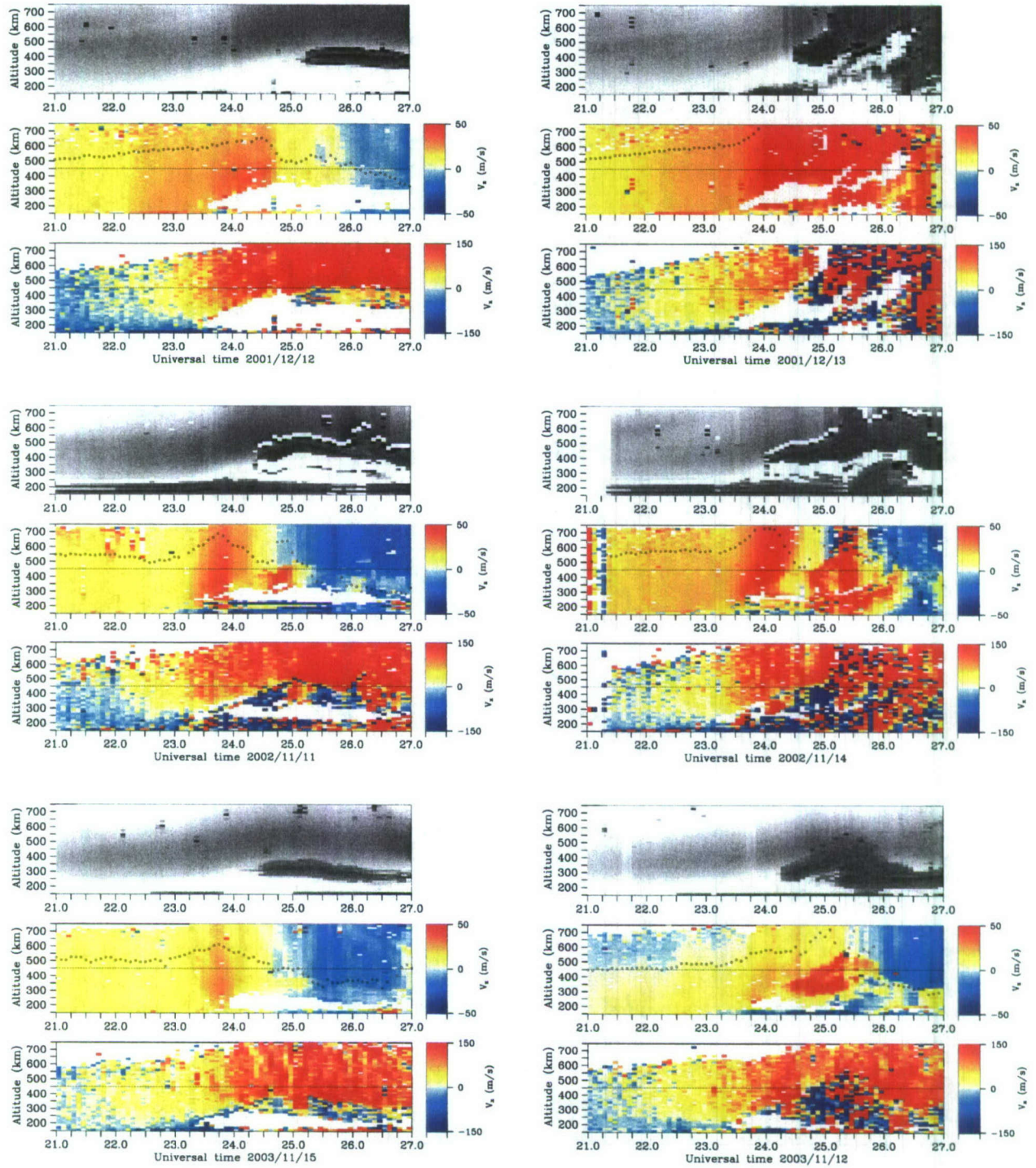


Figure 1: Six examples of ionospheric conditions around twilight. Each example shows the backscatter power (top panel), vertical plasma drift (middle panel), and zonal plasma drift (lower panel), plotted against the scales shown. Symbols plotted in the middle panel represent the vertical drift velocity at 450-km altitude for reference. The left and right columns portray events when topside spread F did not and did occur, respectively. Note that $UT = LT + 5h$.

The existence of seed waves is often postulated to explain the rapid appearance and development of radar plumes and intense plasma irregularities shortly after sunset in the equatorial ionosphere. Gravity waves propagating into the thermosphere may seed the ionosphere as well but are not expected to preferentially excite waves at the observed wavelengths.

Beyond creating conditions for wind-driven instabilities, shear flow may itself destabilize the bottomside F region. Boundary value analyses by [18], [26], and [53] indicated that shear flow generally stabilizes ionospheric interchange instabilities, which was the prevailing sentiment for many years. However, [16], [50], and [15] challenged this idea by pointing out the limitations of boundary value analysis, which is incomplete when applied to non-normal models like those describing sheared flows.

By extending the work of [34] to the equatorial zone, [30] showed that a collisional shear instability may exist in the postsunset ionosphere and be responsible for the precursor waves we observe. In the collisional limit, retrograde plasma motion rather than shear per se drives the instability. However, it is not just an obvious variant of the standard wind-driven interchange instability, since instability occurs when the neutral wind and the background density gradient are normal to one another. The instability is the collisional branch of electrostatic Kelvin Helmholtz and is therefore aptly termed a collisional shear instability. The instability is not damped by collisions and does not require a prereversal enhancement and the elevation of the F layer to function. This may allow it to operate prior to the onset of gravitational interchange instabilities, which are stabilized by collisions, and thereby to serve as a source of seed waves.

An approximate linear growth rate expression for the collisional shear instability was derived in magnetic coordinates (p, q, ϕ) by [31]:

$$\gamma \approx \frac{\kappa_\phi \kappa_p \langle \frac{h_\phi h_q}{h_p} \nu_{in} (u - v_o) n_o' \rangle}{\kappa_\phi^2 \langle \frac{h_p h_q}{h_\phi} \nu_{in} n_o \rangle + \kappa_p^2 \langle \frac{h_\phi h_q}{h_p} \nu_{in} n_o \rangle} \quad (1)$$

where the angle brackets represent averages over a magnetic flux tube as well as over a range of apex altitudes, the prime represents a derivative with respect to the p coordinate, and where the κ terms are constant, nondimensional wavenumbers related to the wavenumber through the appropriate geometric scale factor, e.g. $k_\phi = \kappa_\phi / h_\phi$. The inherently nonlocal nature of the instability prevents the derivation of an exact expression, but the approximation reveals at least how the growth rate scales with background parameters. Remarkably, the possible range of growth rates greatly exceeds that for the generalized Rayleigh Taylor instability, highlighting the importance of this mechanism in the initiation of ESF. Retrograde plasma motion and a steep vertical plasma density gradient in the retrograde stratum are conducive to wave growth. Large flux-tube integrated plasma conductivity suppresses growth. Whether the former overcomes the latter depends on the strength of the neutral wind, the cause of retrograde drifts, and the off-equatorial conductivity distribution.

For example, if the boundary current condition is mainly responsible for retrograde drifts in the bottomside, then the bottomside flux tubes need not be heavily loaded by conductivity in the off-equatorial E and valley regions, and shear instability could be robust. If shear flow is mainly induced by a strong E region dynamo controlling flux tubes in the bottomside, however, then the shear instability would likely be damped. The existence of irregularities in the bottom-type layers gives no clue about which scenario is operating, since they can exist in either case.

Thermospheric wind measurements made by the C/NOFS satellite will be critical for quantifying the shear instability theory. In order to evaluate (1), information about the off-equatorial conductivity distribution will also be

required. This could be provided by a meridional chain of sounders, a bistatic HF sounder link, or by satellite occultation experiments. The same information is required both to quantify the causes of shear flow in the equatorial ionosphere and to evaluate the growth rate of the gravitational interchange instabilities responsible for spread F .

3.2. Jicamarca Incoherent Scatter Data Analysis Using a New Full-Profile Approach

The protracted pre-launch period for C/NOFS has afforded the opportunity to reexamine the analysis of Jicamarca incoherent scatter data used to support spacecraft missions. Incoherent scatter data from a hybrid long-pulse/double-pulse experiment run at Jicamarca during C/NOFS and COSMIC preparatory campaigns have been analyzed using a full-profile analysis stemming from the one described by [24]. In this case, plasma density, electron and ion temperatures, and light ion composition profiles in the topside were estimated simultaneously. Full-profile analysis will be crucial for C/NOFS support at Jicamarca, since the long correlation time of the incoherent scatter signal at 50 MHz invalidates conventional gated analysis of the long-pulse data we plan to collect.

For most of its history, Jicamarca employed a double pulse technique for incoherent scatter experiments [8, 48]. Pairs of short pulses with opposite circular polarizations were transmitted, and lag product matrices were assembled from the backscatter, one lag at a time. The size of the scattering volume was set by the pulse lengths rather than the lag spacing, and problems associated with inhomogeneity were thereby avoided. The double pulse experiment was also relatively immune to clutter from the ground, the equatorial electrojet, and other sources. Faraday rotation measurements using phase information from the orthogonal polarizations yielded an independent measurement of absolute electron density for calibration purposes [7]. However, the double pulse experiment was very slow and did not fully exploit the average power limitations of the transmitters. Given reasonable incoherent integration times, the experiment could not yield useful ionospheric profiles at protonospheric heights.

More recently, a hybrid experiment combining the double pulses with an alternating code was implemented at Jicamarca [27]. The alternating code permits the estimation of the lag product matrix with range resolution set by the bit length of the code rather than the pulse length [41, 42, 43]. The range resolution of all the lags is uniform except for the zero lag. The alternating code thus resolves many analysis problems associated with inhomogeneity. The alternating code is also much faster than the double pulse, providing multiple lag product estimates from each pulse and fully utilizing the duty cycles of the transmitters. Given reasonable incoherent integration times, the hybrid experiment yields useful ionospheric profiles well into the protonosphere.

While representing an improvement over the double pulse at altitudes where it can be applied, the alternating code is still less sensitive than the long pulse. This is because most of the signal in a given receiver sample comes from ranges other than the range under analysis. The experiment is self clutter prone, with a signal-to-clutter ratio never exceeding the reciprocal of the code length. Added clutter is the price paid for reduced range ambiguity.

We, therefore, pursued a new strategy for long-pulse analysis introduced by [24] and investigated by [44]. Rather than manipulating the lag products from a long-pulse experiment, constructing approximations of autocorrelation functions, and fitting the results for ionospheric parameters one range at a time (so-called "gated" analysis), [24] proposed the simultaneous estimation of complete parameter profiles directly from the lag product matrices as they are measured.

The technique is termed “full profile analysis” and belongs to a class of problems in statistical inverse theory. The technique neither degrades the data using summation rules nor introduces clutter with pulse coding. In practice, it entails solving the forward model iteratively until a cost function composed of the model prediction error (essentially, the chi-squared statistic) and a combination of model metrics is minimized.

The theory that relates the autocorrelation function $\rho(k, \tau; r)$ to the state variables of the ionospheric plasma (electron density, electron and ion temperatures, ion composition, drifts, etc.) is well known and need not be reviewed here (see for example [4, 9, 5, 57, 11, 12, 13, 51, 52, 23, 60]). Application of the theory at Jicamarca is complicated by the small magnetic dip angle, however. A considerable body of work exploring the theory at small aspect angles has emerged in recent years. Here, we highlight findings relevant to the forward model.

[36] first noted that the incoherent scatter spectrum at small aspect angles is even smaller than the standard theory predicts. (See also [38].) At the same time, it had long been known that the standard theory failed to predict the correct electron-ion temperature ratio for finite but small aspect angles, of the order of a few degrees or less [48]. [56] were able to account for both of these phenomena (qualitatively for the former and quantitatively for the latter) by including the effects of electron Coulomb collisions in the calculation of the electron admittance. Their calculations were based on Monte Carlo simulations. Summarizing these findings, [1] went on to show that the new Coulomb collision corrections bring temperature ratio observations made a few degrees off perpendicular at Jicamarca into compliance with expectation. Those corrections, which have been made available in tabular form (M. Sulzer, personal communication) are incorporated in the present analysis.

A second issue involves the relationship between plasma density, the radar scattering cross-section, and power profile measurements. At small aspect angles, the incoherent scatter cross section depends on the electron and ion temperatures and the plasma density in a complicated way not predicted by the approximation for large aspect angles given by [6] employed widely at other ISR facilities. [46] have examined the effect in detail, including for the first time the effects of electron Coulomb collisions in their calculations. Extending the work by [61], they incorporate the effects of Coulomb collisions analytically with the introduction of a heuristic operator in the so-called Gordeyev integral which, when evaluated numerically, reproduces the results of [56]. [49] recently used their results to convert Jicamarca power profiles to density profiles, finding good agreement with Faraday rotation measurements. We adopt the same methodology here, making use of Faraday rotation only for absolute density calibration.

Full profile analysis is an example of a discrete inverse problem of the form $G(m) = d$, where d is a column vector representing known data, m is a column vector representing unknown model parameters, and G is the known theory relating them. In this instance, the data are lag profile estimates, the model parameters are plasma density, temperature and composition specified at various altitudes, and the theory is incoherent scatter theory combined with the radar ambiguity function. If the model is linear or its estimate m^{est} is sufficiently close to the solution that the theory can be linearized about m^{est} , then the problem becomes simply $Gm^{\text{est}} = d$, where $d \in R^n$, $m \in R^m$, and $G \in R^{n \times m}$. The apparent simplicity of even this problem is deceptive, and its solution in the presence of noisy data almost inevitably necessitates recourse to statistical inverse methods. For an introduction to inverse methodology, consult for example [45], [58], and [2].

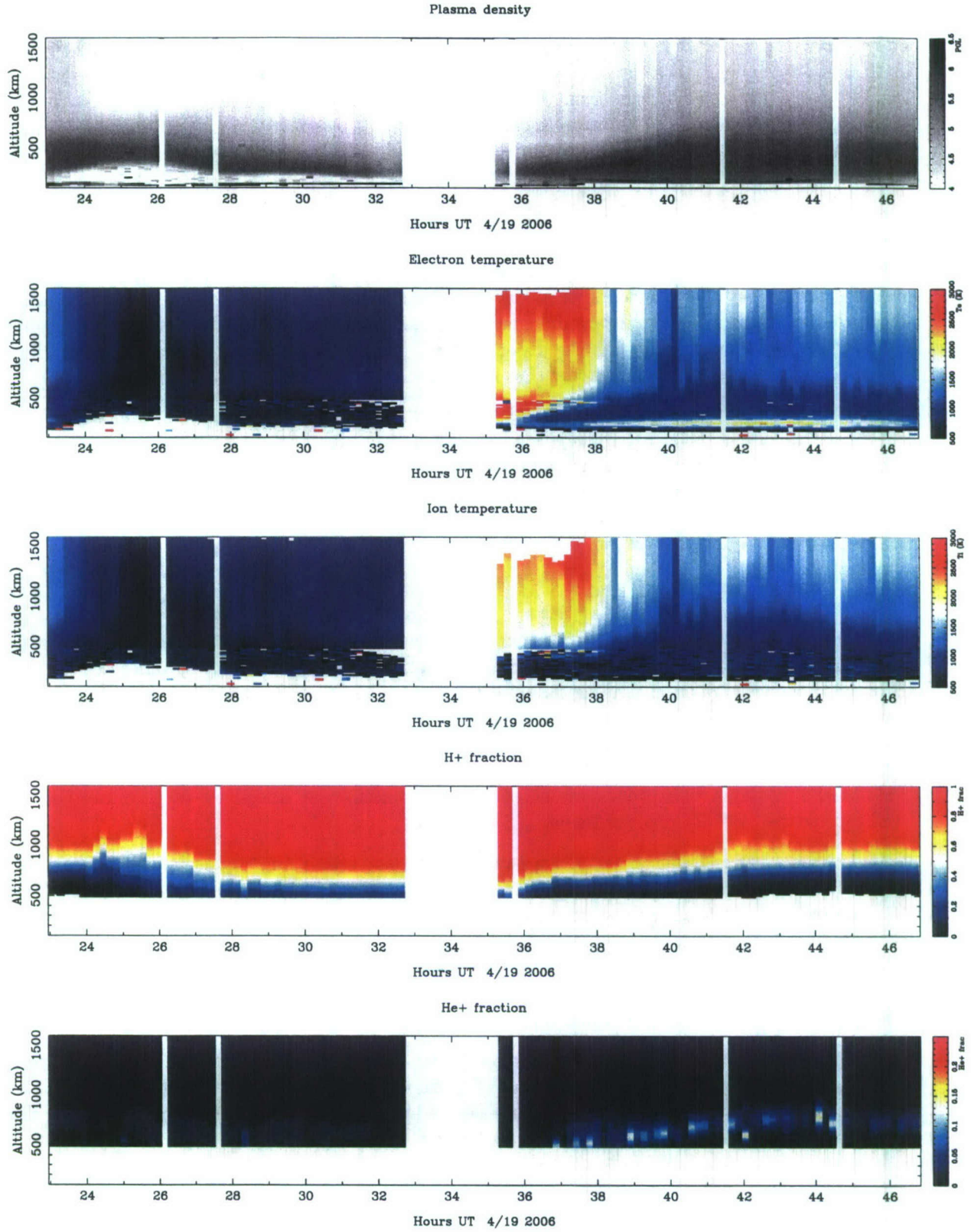


Figure 2: Summary Jicamarca data for the full profile analysis. From top to bottom, the panels represent electron density, electron temperature, ion temperature, hydrogen ion fraction, and helium ion fraction (25% full scale). A data gap exists between 03–06 LT when the galaxy was directly over the radar.

Zero lag inversion In the present problem, each of the measured long-pulse lag products represents the two dimensional convolution of the radar range-time ambiguity function and the auto-correlation function of the scattering medium. The zero lag is no exception. However, since the ACF is nearly uniform over the small delays τ entering into the problem, we can regard the zero lag as the one-dimensional correlation of a 'true' power profile with the emitted radar pulse shape to a good approximation. Here, 'true' means the profile that would be measured ideally if short pulses were used. We can therefore recover the former by deconvolving the latter from the zero lag profile.

Deconvolution is performed using Tikhonov regularization. This is accomplished with augmented linear least squares minimization, the fourth enumerated strategy above. Minimization is performed using a non-negative least squares (NNLS) routine that prevents the occurrence of negative results anywhere in the deconvolved profile [40]. This strategy enhances the stability and robustness of the methods and permits smaller regularization parameters than would otherwise be possible. It is noteworthy that the droop in transmitter power that occurs during long pulse transmission produces a forward model that is better conditioned than would be a uniform pulse.

The 'true' power profile combined with incoherent scatter theory and the shape of the radar pulse complete the forward model. Given specifications for the ionospheric density, temperature, and composition profiles along with the radar range-time ambiguity function, we can predict the absolute lag product matrix. In practice, the integrals in the ambiguity function are evaluated discretely using a trapezoidal rule. The proxy electron density profile is a sufficiently good approximation for n_e for all forward modeling intents and purposes and need only be corrected at the conclusion of the analysis.

Inverting the entire lag profile matrix For the forward model, electron temperature, the electron/ion temperature ratio, and the hydrogen and helium ion fractions are specified coarsely at 20 uniformly-spaced ranges spanning the solution space. These become the knots used for cubic B-spline interpolation [3]. The interpolated functions thus created are twice-differentiable continuous and provide a means of specifying the ionospheric parameter profiles with arbitrarily fine resolution for forward modeling. Computing the B-spline coefficients is fast and efficient, and experimentation has shown that the topside profiles measured with conventional gated analysis at Jicamarca can be well represented with 20 or fewer knots.

The model parameters, the 4×20 knot values, are calculated using augmented nonlinear least squares minimization. The minimization algorithm is conventional Levenberg-Marquardt. The parameters are initialized with values resulting from an extensive grid search when a large family of representative trial profiles are generated and a χ^2 statistic calculated for each. It is generally possible to find initial profiles this way for which $\chi^2/m < 5$, m being the number of parameters. Levenberg Marquardt iteration generally yields final values for $\chi^2/m \sim 2-3$. Smaller values can be produced only at the cost of producing very irregular parameter profiles.

Augmentation in this case means introducing six additional cost functions that help to regularize the output of the algorithm. Each of these is multiplied by an adjustable weight. The weights have been set so as to inhibit results that are inconsistent with general expectations for the ionosphere. The cost functions are enumerated below.

1. $\langle |d^2 T_e / dz^2| \rangle$

2. $\langle |d^2 T_i / dz^2| \rangle$
3. $\langle |d^2 \tilde{H}^+ / dz^2| \rangle$
4. $\exp(-\min(0, 1 - H^+ - He^+))$
5. $\langle He^+ \rangle$
6. $\exp(-\min(0, T_e - T_i))$

The first three cost functions pertain to the global range averages of the second derivatives of the electron temperature, ion temperature, and hydrogen ion fractions, respectively. Suppressing these quantities inhibits spurious oscillations in the profiles associated with poor conditioning. Note that the net hydrogen fraction in our algorithm is defined by

$$H^+ = (1 + \tanh \tilde{H}^+)/2$$

A similar function is used to express the helium ion fraction. The functions restrict the ion fractions to values between 0 and 1. It remains possible for the combined hydrogen and helium ion fractions to exceed unity, and so a fourth cost function was introduced to inhibit this.

A fifth cost function is a very weak prohibition of helium ions overall. This is meant to prevent the algorithm from producing spurious He^+ layers that might otherwise come about as a consequence of any systemic errors in data acquisition and processing. Helium ions indicated by the full profile analysis must be pointed to by clear signatures in the lag product data. Finally, a sixth cost function is a prohibition against electron-to-ion temperature ratios less than unity. This is a condition that we expect never to occur in nature, and the cost function prevents the full profile algorithm from exploring that region of solution space.

Twenty-four hours of hybrid double/long-pulse data were taken during April 19–20, 2006, at Jicamarca and processed using the full-profile algorithm. In the analysis, only the diagonal components of the error covariance matrices were used. While the formalism surrounding the calculation and incorporation of the complete covariance matrix is straightforward, the storage and computational demands are significant, and sparse matrix solvers are required in practice. Sparse matrix math has yet to be incorporated in our algorithm.

Processed data appear in the summary plot shown in Fig. 2 for the 24-hour run. Data between 0300–0600 LT when the galaxy was inside the antenna beam have been excised, as have intervals when residual echoes from space debris interfered with the analysis. While there is significant scatter in some of the parameters, particularly in the postsunrise temperatures, this is a consequence of low signal levels and consistent with our error analysis.

The salient features of Fig. 2 are the dramatic electron heating after sunrise, the low and relatively constant O^+/H^+ transition height, and the appearance of a thin, patchy helium layer in the morning. They are remarkably similar to model predictions for equinox solar minimum conditions over Jicamarca made by [25] except that the measured plasma temperatures are somewhat smaller at sunrise. These features have also been suggested by gated analyses in the past and so do not appear to be creations of the full-profile analysis.

Full-profile analysis is now available for C/NOFS CalVal. Furthermore, it can and should be used as a baseline against which to tune and validate model ionospheres such as the one under development at AFRL. The full-profile results (density, temperature, and composition profiles) are the most reliable representation of the background equatorial ionosphere available to date.

3.3. Optimal Radio Occultation Profile Inversion

Radio occultation measurements of the Earth's atmosphere and ionosphere using global positioning satellites and receivers placed on satellites in low Earth orbit (LEO) are an important new source of remote sensing information, supplementing ground-based and in situ measurements and serving as sources for assimilative models. The COSMIC mission in particular is dedicated to specifying the ionosphere globally for purposes of assimilative modeling and stability forecasting. Developed for planetary atmospheric research (e.g., [47, 14]), the radio occultation technique involves inferring gradients in the index of refraction from differential phase measurements and the implied optical path length between transmitting and receiving satellites. The index of refraction in the Earth's atmosphere is a function of temperature, pressure, water and water vapor content, and electron density, where the last factor has by far the most significant effect. Inferring total electron content (TEC) on the ray path between the satellites is then a relatively straightforward task. Reviews of different analysis techniques have been given by [39] and [54].

The purpose of this project was to investigate a pathology that arises in the conventional inversion strategy and explore means of mitigation. Two conceptually related methodologies, Tikhonov regularization and maximum entropy, were described and compared. While both offer substantial improvement over straight linear inverse transformation, the latter was seen to outperform the former in its ability to retain fine structure while suppressing artifacts.

We are interested in the specific problem of recovering altitude profiles of ionospheric electric density from radio occultation observations made with satellite pairs. We assume spherical symmetry so that the electron density is a function of altitude r alone. We further neglect ray bending and birefringence in this analysis and consider only the effect that the ionospheric plasma has on straight-line propagation through variations in the index of refraction n :

$$n = 1 - 80.48 \frac{n_e}{f^2}$$

where n_e is the electron number density in MKS units and f is the radio frequency in Hertz, which is taken to be well above the critical frequency in the ionosphere. Because of the dispersion, signals received at different frequencies will have different optical path lengths and arrive out of phase. For a given propagation path with closest approach (to the center of the Earth) s , the phase difference will be related to the electron density profile through Abel's transform:

$$\phi(s) = 2C \int_s^\infty n_e(r) \frac{r dr}{\sqrt{r^2 - s^2}} \quad (2)$$

where it is assumed that both the transmission and reception points are above the altitudes where significant electron density exists. (This will not generally be true for LEO satellites, but a modified methodology exists in that case that uses positive and negative elevation rays to resolve the problem [21].) Here, the constant C for the two frequencies f_1 and f_2 is $2\pi(f_1 - f_2)/(cf_1 f_2)$. (i.e. not the speed of light). As the satellites move, they sweep out the continuous curves $\phi(s)$. The task is to recover the electron density profile $n_e(r)$ by inverting (2).

In the event that $n_e(r)$ decreases more rapidly than r^{-1} at the upper bound, the inverse of (2) exists:

$$n_e(r) = -\frac{1}{\pi C} \int_r^\infty \frac{d\phi}{ds} \frac{ds}{\sqrt{s^2 - r^2}} \quad (3)$$

This transformation has the added benefit of acting on the derivative of the phase term, sidestepping ambiguities associated with absolute phase measurement. It is a straightforward matter to evaluate (3) using standard numerical integration techniques. We will see that the problem is well posed and that (3) implies no systematic distortion of the desired profile. However, (3) possesses a certain pathology that makes it poorly suited for ionospheric investigation. That pathology and a remedy are described below.

Consider the discrete versions of (2) and (3). The electron density and phase difference profiles can be discretized spatially and regarded as column vectors. We designate the phases with the vector d for data and the electron densities with the vector m for model. Let d be specified at n points and m at m points, where the integers n and m need not be equal. The integrals can then be carried out using summation rules. A simple trapezoidal integration scheme will be used here, although higher order schemes are certainly possible. The derivative in (3) can be evaluated with backward differencing. Finally, the forward and inverse transforms assume the form

$$d = Gm \quad (4)$$

$$\hat{m} = G^\dagger d \quad (5)$$

where G is the $n \times m$ linear transformation implied by the integral in (2) and G^\dagger is its $m \times n$ generalized inverse. The caret in (5) denotes an estimate with accuracy depending on the qualities of G^\dagger ; note that G^\dagger need not and will not in general be G^{-1} . The way forward is the subject of inverse theory, which is described in a number of standard texts (see for example [2], [45], and [58]). Using the Moore-Penrose generalized inverse and given

$$G = U_p S_p V_p^t, \quad (6)$$

$$G^\dagger = V_p S_p^{-1} U_p^t \quad (7)$$

where U_p , S_p , and V_p are matrices found through the singular value decomposition of G , truncated to dimensions limited by the rank p of G . Here, U_p and V_p are orthogonal matrices (size $n \times p$ and $m \times p$, respectively) spanning the data and model ranges, respectively, and S_p is the $p \times p$ diagonal matrix composed of positive definite singular values.

For the purposes of this analysis, it will suffice to consider the even determined case in which G is full rank and $p = m = n$. Then the singular values are all nonzero, $V_p V_p^t = U_p U_p^t = I$, and

$$\begin{aligned} G^\dagger &= V S^{-1} U^t \\ &= (U S V^t)^{-1} \\ &= G^{-1} \end{aligned} \quad (8)$$

The inverse is unique and exact, since $\hat{m} = G^\dagger G m = m$.

The accuracy of the model estimate in the presence of noise depends on the stability of the inversion and is the issue motivating this analysis. The structure of (8) gives an indication. Here, the inverse operator can be seen to decompose the data vector into its component singular vectors and to scale each one by the corresponding inverse singular value. Ill-conditioned problems are signaled by ratios of the smallest-to-largest singular values competing with the floating point precision of the computer, since roundoff error prohibits accurate retention of all the singular modes, leading to instability. For the Abel inversion, this ratio is just comparable to n . Even so, this suggests that error amplification will be substantially different for different kinds of features in the data. This phenomenon can be explored further through an example.

Fig. 3 illustrates the performance of the Abel transform inversion by applying the linear transformation in (5) to simulated data. For these simulations, $n = m = 60$. Panel (a) shows the initial electron density profile, $n_e(r)$, discretized on a grid with unit spacing. The electron density here is dimensionless and normalized such that the area under the curve is also unity. The profile is composed of three Maxwellian components and is intended to vaguely resemble the ionosphere.

Panel (b) shows simulated occultation data $\phi(s)$ computed using the transformation in (4). For these calculations, we take the constant C in (2) and (3) to be unity for simplicity. Two curves are shown in panel (b), one without added noise, and one with noise added. The error bars reflect the amplitude of the noise, which is independent Gaussian random noise with a standard deviation $\sigma = 0.04$. To our knowledge, there is nothing that prevents correlated measurement errors in radio occultation experiments (see below). However, the results here are easily generalized for the case of nonuniform and correlated errors.

Panel (c) shows the results of model inversion using the linear transformation in (5). Results for the noisy and noise-free cases are shown with solid and dashed lines, respectively. The noise-free inversion is indistinguishable from the original density profile. Error bars for the noisy case were computed using the standard error propagation formula:

$$C_m = G^\dagger C_d (G^\dagger)^t \quad (9)$$

The problem with the inverse method adopted so far is error propagation. The model inversion in panel (c) of Fig. 3 exhibits large fluctuations and wide confidence intervals despite the modest amount of noise added to the simulated data. The problem grows with decreasing range to the point of introducing artificial layers and negative-going excursions. The negative excursions and layers that might easily be confused with intermediate or sporadic E layers in nature are unacceptable artifacts and render direct linear transformation suboptimal.

The cause of the problem is illustrated by panel (d) of Fig. 3. The histograms represent the singular values of G , ranked top to bottom from largest to smallest. The condition number of the inverse transform can be calculated from the ratio of the largest to smallest of the singular values. That ratio is approximately n in this problem. While that is not large enough to give rise to numerical instability, it has serious consequences for error amplification. Also shown in panel (d) are the singular vectors with the two largest and two smallest singular values. Large (small) singular values correspond to unstructured (highly structured) singular vectors with most of their content at large (small) ranges. Features that resemble the structured singular vectors in the noisy data will be amplified much more than features that resemble the unstructured ones. This explains the preponderance of noise amplification and ragged oscillations in the model inversion at low ranges. The behavior is an inherent feature of the inverse Abel transform.

Two conventional strategies exist for mitigating the oscillatory behavior of the linear inversion. The first is to truncate the singular value matrix, regarding as zero those values that fall below some threshold. The corresponding, problematic singular vectors and associated noise amplification behavior are thus eliminated. A less drastic approach is to filter the singular values, modifying them artificially so that they do not assume too low values. Such so-called damped SVD methods include the method of Tikhonov regularization. Panel (e) in Fig. 3 shows a regularized version of the model inversion with error bars recalculated according to (9). The forward and inverse models in (6) were recalculated after dividing the singular values λ_i by the filter coefficients

$$f_i = \frac{\lambda_i^2}{\lambda_i^2 + \alpha^2} \quad (10)$$

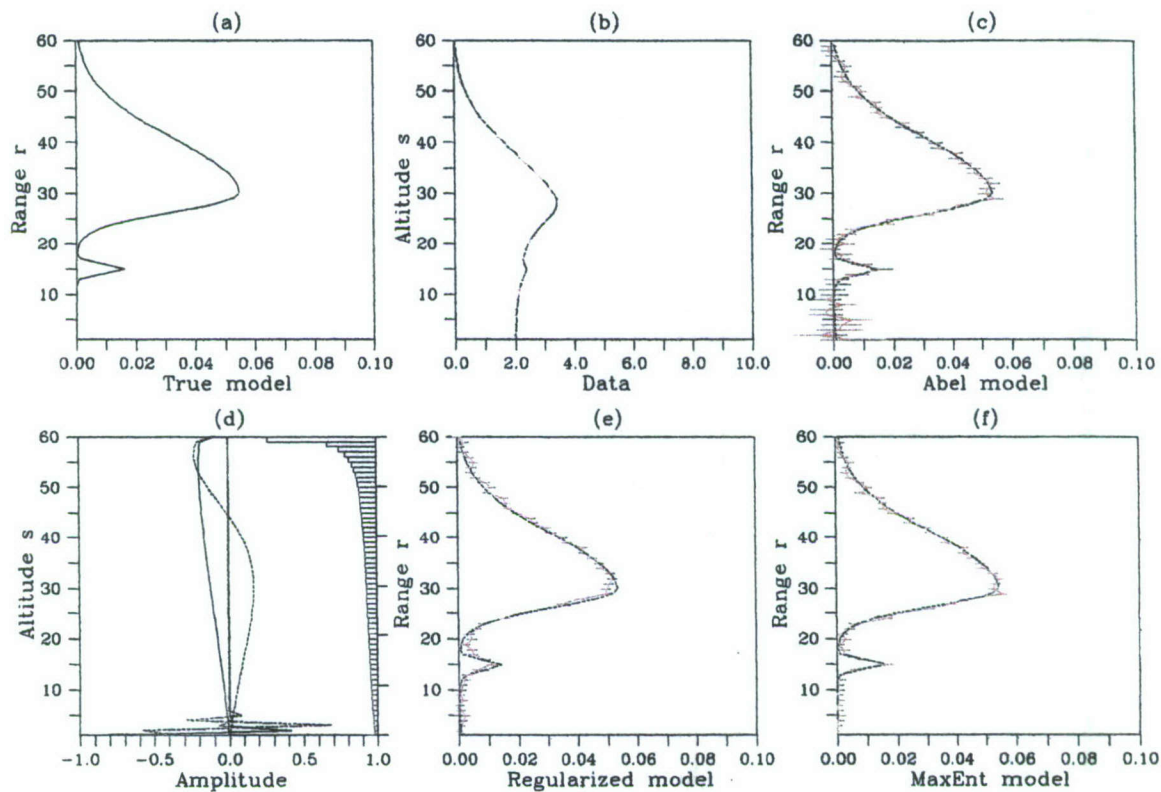


Figure 3: Example occultation profile inversion comparing different methods. (a) Simulated "true" electron density profile $n_e(r)$. (b) Phase profile $\phi(s)$ calculated using (4). Simulated phase data with (solid) and without (dashed) noise are shown. (c) Direct linear inversion of the simulated data using (5). Models with (solid) and without (dashed) noise are shown. (d) Singular value analysis of the linear transformation (see text). (e) Linear inversion using Tikhonov regularization. The dashed line is the true model. (f) Results obtained using maximum entropy. The dashed line is the true model.

where α is the regularization parameter. This is equivalent to finding the model that minimizes a weighted combination of the L_2 norms of the noisy data prediction error $G\hat{m} - d$ and the model itself \hat{m} . The regularization parameter was set to 10 in this example in an attempt to reduce artifacts while retaining fine structure. While the results are superior to the unregularized model in terms of having smaller uncertainties and fewer sporadic oscillations, the profile in (e) is clearly distorted, the peaks being rounded and the valley being filled in. Note that while a non-negativity constraint can be incorporated into regularization, we have not done so here.

Another candidate for the prior probability of a model is its entropy, a combinatorial measure from which partition functions in statistical mechanics are constructed. Entropy is also a measure of information content [55]. A model high in entropy has a high probability of occurrence, all other things being equal, and represents minimal independent information, making it minimally committal to unmeasured data. A preference for high-entropy models suppresses artifacts, since every feature in the model must be supported by the data.

In the maximum entropy problem, the prior probability is made to be a function of the entropy (usually e^S). This step can be somewhat controversial, as entropy lies outside the narrow, frequentist definition of probability, having more to do with the prior state of knowledge and the plausibility of the model. As [17] points out, frequencies are difficult to obtain in scientific measurements, particularly exploratory ones like those of interest here. However, [33] and others have argued that Bayes theorem applies equally well to theoretical probabilities based on information theory as to frequencies. Numerical simulations offer a means of testing the argument.

We have performed the occultation profile inversion using the algorithm described recently by [29]. Results are shown in panel (f) of Fig. 3. The inversion appears to produce an unbiased reproduction of the original density profile, even in the vicinity of sharp peaks and steep gradients. The recovered density approaches but never crosses zero at the layer boundaries. The overall behavior is superior to the Tikhonov regularization solution for any choice of regularization parameter α . Evidently, the noisy data contained sufficient information to specify the presence of steep peaks and shallow valleys in the profile. The constraint that the model be positive definite and in some sense smooth was sufficient to suppress spurious layers and other artifacts without any artificial truncation of the model space. Similar results are obtained for different profile shapes, noise levels, and model sizes.

The purpose of this study was to illustrate some shortcomings of standard, direct, linear inversion of radio occultation data and to compare and contrast two common alternative approaches, Tikhonov regularization and maximum entropy. Both reduce the production of spurious layers and artifacts at low altitudes inherent in the structure of the inverse Abel transform. The former is a fixed linear filter that works by attenuating singular modes which tend to amplify noise. The danger with this approach is that it necessarily removes fine structure and distorts the model profile. The latter is an adaptive nonlinear filter which suppresses features in the model that are not supported in the data. Maximum entropy produces positive definite models which retain their fine structure and exhibit little distortion.

It is imperative that direct linear inversion of radio occultation profiles not be part of any operational use of data from the COSMIC or other satellite mission. Artifacts in the standard inversion scheme take the form of convincing layers at low altitudes which will certainly be misinterpreted as sporadic E , intermediate, or bottomside layers. This problem can be avoided by incorporating regularization or, better still, by using a Bayesian inversion strategy based on an entropy metric.

4. BIBLIOGRAPHY

References

- [1] N. Aponte, M. P. Sulzer, and S. A. Gonzales. Correction of the Jicamarca electron-ion temperature ratio problem: verifying the effect of electron Coulomb collisions on the incoherent scatter spectrum. *J. Geophys. Res.*, 2001.
- [2] R. C. Aster, B. Borchers, and C. H. Thurber. *Parameter Estimation and Inverse Problems*. Elsevier, New York, 2005.
- [3] C. De-Boor. *A Practical Guide to Splines*. Springer Verlag, New York, 1978.
- [4] J. P. Dougherty and D. T. Farley. A theory of incoherent scattering of radio waves by a plasma. *Proc. Roy. Soc.*, A259:79, 1960.
- [5] J. P. Dougherty and D. T. Farley. A theory of incoherent scattering of radio waves by a plasma, 3, scattering in a partly ionized gas. *J. Geophys. Res.*, 68:5473, 1963.
- [6] D. T. Farley. A theory of incoherent scattering of radio waves by a plasma, 4, The effect of unequal ion and electron temperatures. *J. Geophys. Res.*, 71:4091, 1966.
- [7] D. T. Farley. Faraday rotation measurements using incoherent scatter. *Radio Sci.*, 4:935, 1969.
- [8] D. T. Farley. Incoherent scatter correlation function measurements. *Radio Sci.*, 4:935, 1969.
- [9] D. T. Farley, J. P. Dougherty, and D. W. Barron. A theory of incoherent scattering of radio waves by a plasma, 2, Scattering in a magnetic field. *Proc. R. Soc.*, London Ser. A, 263:238, 1961.
- [10] B. G. Fejer. The equatorial ionospheric electric fields. A review. *J. Atmos. Terr. Phys.*, 43:377, 1981.
- [11] J. A. Fejer. Radio wave scattering by an ionized gas in thermal equilibrium. *J. Geophys. Res.*, 81:3441, 1960.
- [12] J. A. Fejer. Scattering of radio wave by an ionized gas in thermal equilibrium. *Can. J. Phys.*, 38:1114, 1960.
- [13] J. A. Fejer. Radio wave scattering by an ionized gas in thermal equilibrium in the presence of a uniform magnetic field. *Can. J. Phys.*, 39:716, 1961.
- [14] G. Fjeldbo, A. J. Kliore, and V. R. Eshleman. The neutral atmosphere of Venus studied with the Mariner V radio occultation experiments. *Astron. J.*, 76(2):123, 1971.
- [15] J. P. Flaherty, C. E. Seyler, and L. N. Trefethen. Large-amplitude transient growth in the linear evolution of equatorial spread F with a sheared zonal flow. *J. Geophys. Res.*, 104:6843, 1999.
- [16] Z. F. Fu, L. C. Lee, and J. D. Huba. A quasi-local theory of the $\mathbf{E} \times \mathbf{B}$ instability in the ionosphere. *J. Geophys. Res.*, 91:3263, 1986.

- [17] C. J. Gilmore. Maximum entropy and Bayesian statistics in crystallography: a review of practical applications. *Acta Cryst.*, A52:561, 1996.
- [18] P. N. Guzdar, P. Satyanarayana, J. D. Huba, and S. L. Ossakow. Influence of velocity shear on Rayleigh-Taylor instability. *Geophys. Res. Lett.*, 9:547, 1983.
- [19] G. Haerendel and J. V. Eccles. The role of the equatorial electrojet in the evening ionosphere. *J. Geophys. Res.*, 97:1181, 1992.
- [20] G. Haerendel, J. V. Eccles, and S. Cakir. Theory for modeling the equatorial evening ionosphere and the origin of the shear in the horizontal plasma flow. *J. Geophys. Res.*, 97:1209, 1992.
- [21] S. B. Healy, J. Haase, and O. Lesne. Abel transform inversion of radio occultation measurements made with a receiver inside Earth's atmosphere. *Ann. Geophys.*, 20:1253, 2002.
- [22] R. A. Heelis, P. C. Kendall, R. J. Moffet, D.W. Windle, and H. Rishbeth. Electric coupling of the *E* and *F* regions and its effect of the *F* region drifts and winds. *Planet. Space Sci.*, 22:743, 1974.
- [23] T. Hogfors. Density fluctuations in a plasma in a magnetic field, with applications to the ionosphere. *J. Geophys. Res.*, 66:1699, 1961.
- [24] J. M. Holt, D. A. Rhoda, D. Tetenbaum, and A. P. van Eyken. Optimal analysis of incoherent scatter radar data. *Radio Sci.*, 27:435, 1992.
- [25] J. D. Huba, G. Joyce, and J. A. Fedder. Sami2 is another model of the ionosphere (SAMI2): A new low-latitude ionospheric model. *J. Geophys. Res.*, 105:23,035, 2000.
- [26] J. D. Huba and L. C. Lee. Short wavelength stabilization of the gradient drift instability due to velocity shear. *Geophys. Res. Lett.*, 10:357, 1983.
- [27] D. L. Hysell. Incoherent scatter experiments at Jicamarca using alternating codes. *Radio Sci.*, 35:1425, 2000.
- [28] D. L. Hysell. Inverting ionospheric radio occultation measurements using maximum entropy. *Radio Sci.*, 42:RS4022, doi:10.1029/2007RS003635, 2007.
- [29] D. L. Hysell and J. L. Chau. Optimal aperture synthesis radar imaging. *Radio Sci.*, 41:10.1029/2005RS003383, RS2003, 2006.
- [30] D. L. Hysell and E. Kudeki. Collisional shear instability in the equatorial *F* region ionosphere. *J. Geophys. Res.*, 109:(A11301), 2004.
- [31] D. L. Hysell, E. Kudeki, and J. L. Chau. Possible ionospheric preconditioning by shear flow leading to equatorial spread *F*. *Ann. Geophys.*, 23:2647, 2005.
- [32] D. L. Hysell, F. S. Rodrigues, J. L. Chau, and J. Huba. Full profile incoherent scatter analysis at Jicamarca. *Ann. Geophys.*, 2007. submitted.
- [33] E. T. Jaynes. Where do we stand of maximum entropy? In R. D. Levine and M. Tribus, editors, *The Maximum Entropy Formalism*, pages 15–118. Cambridge: MIT Press, 1979.
- [34] M. J. Keskinen, H. G. Mitchell, J. A. Fedder, P. Satyanarayana, S. T. Zalesak, and J. D. Huba. Nonlinear evolution of the Kelvin-Helmholtz instability in the high-latitude ionosphere. *J. Geophys. Res.*, 93:137, 1988.

- [35] E. Kudeki and S. Bhattacharyya. Post-sunset vortex in equatorial F -region plasma drifts and implications for bottomside spread- F . *J. Geophys. Res.*, 104:28,163, 1999.
- [36] E. Kudeki, S. Bhattacharyya, and R. F. Woodman. A new approach in incoherent scatter F region $E \times B$ drift measurements at Jicamarca. *J. Geophys. Res.*, 104:28,145, 1999.
- [37] E. Kudeki, B. G. Fejer, D. T. Farley, and H. M. Ierke. Interferometer studies of equatorial F region irregularities and drifts. *Geophys. Res. Lett.*, 8:377, 1981.
- [38] E. Kudeki and M. Milla. Incoherent scatter spectrum theory for modes propagating perpendicular to the geomagnetic field. *J. Geophys. Res.*, 111, A06306:DOI:10.1029/2005JA011, 2006.
- [39] E. R. Kursinski, G. A. Haa, K. R. Hardy, J. T. Schofield, and R. Linfield. Observing Earth's atmosphere with radio occultation measurements using GPS. *J. Geophys. Res.*, 102(D19):23,429, 1997.
- [40] C. W. Lawson and R. J. Hanson. *Solving Least Squares Problems*. SIAM, 1987.
- [41] M. S. Lehtinen. Statistical theory of incoherent scatter radar measurements. Technical Report 86/45, Eur. Incoherent Scatter Sci. Assoc., Kiruna, Sweden, 1986.
- [42] M. S. Lehtinen and I. Häggström. A new modulation principle for incoherent scatter measurements. *Radio Sci.*, 22:625, 1987.
- [43] M. S. Lehtinen and A. Huuskonen. General incoherent scatter analysis and GUISDAP. *J. Atmos. Terr. Phys.*, 58:435, 1996.
- [44] M. S. Lehtinen, A. Huuskonen, and J. Pirttilä. First experiences of full-profile analysis with GUISDAP. *Ann. Geophys.*, 1996.
- [45] W. Menke. *Geophysical Data Analysis: Discrete Inverse Theory*. Academic, New York, 1984.
- [46] M. Milla and E. Kudeki. F -region electron density and Te/Ti measurements using incoherent scatter power data collected at ALTAIR. *Ann. Geophys.*, page 1333, 2006.
- [47] R. A. Phinney and D. L. Anderson. On the radio occultation method for studying planetary atmospheres. *J. Geophys. Res.*, 73(5):1819, 1968.
- [48] J. E. Pingree. *Incoherent scatter measurements and inferred energy fluxes in the equatorial F -region ionosphere*. PhD thesis, Cornell Univ., Ithaca, N. Y., 1990.
- [49] F. S. Rodrigues, M. J. Nicolls, and D. L. Hysell. Improved electron density measurements at Jicamarca. *J. Geophys. Res.*, 2007. submitted.
- [50] C. Ronchi, P. L. Simion, and R. N. Sudan. A nonlocal linear theory of the gradient drift instability in the equatorial electrojet. *J. Geophys. Res.*, 94:1317, 1989.
- [51] E. E. Salpeter. Electron density fluctuations in a plasma. *Phys. Rev.*, 120:1528, 1960.
- [52] E. E. Salpeter. Plasma density fluctuations in a magnetic field. *Phys. Rev.*, 122:1663, 1961.
- [53] P. Satyanarayana, P. N. Guzdar, J. D. Huba, and S. L. Ossakow. Rayleigh-Taylor instability in the presence of a stratified shear layer. *J. Geophys. Res.*, 89:2945, 1984.

- [54] W. S. Schreiner, S. V. Sokolovskiy, C. Rocken, and D. C. Hunt. Analysis and validation of GPS/MET radio occultation data in the ionosphere. *Radio Sci.*, 34(4):949, 1999.
- [55] C. E. Shannon and W. Weaver. *The Mathematical Theory of Communication*. Univ. of Ill. Press, Urbana, 1949.
- [56] M. P. Sulzer and S. Gonzalez. The effect of electron Coulomb collisions on the incoherent scatter spectrum in the F region at Jicamarca. *J. Geophys. Res.*, 104:22,535, 1999.
- [57] W. E. Swartz and D. T. Farley. A theory of incoherent scattering of radiowaves by a plasma, 5, The use of the Nyquist theorem in general quasi-equilibrium situations. *J. Geophys. Res.*, 84:1930, 1979.
- [58] A. Tarantola. *Inverse Theory*. Elsevier, New York, 1987.
- [59] R. T. Tsunoda, R. C. Livingston, and C. L. Rino. Evidence of a velocity shear in bulk plasma motion associated with the post-sunset rise of the equatorial F layer. *Geophys. Res. Lett.*, 8:807, 1981.
- [60] R. F. Woodman. *Incoherent scattering of electromagnetic waves by a plasma*. PhD thesis, Harvard University, 1967.
- [61] R. F. Woodman. On a proper electron collision frequency for a Fokker-Planck collision model with Jicamarca applications. *J. Atmos. Sol. Terr. Phys.*, 2004.